



Contents lists available at ScienceDirect

Journal of Science: Advanced Materials and Devices

journal homepage: www.elsevier.com/locate/jsamd

Original Article

An integrated microfluidic concentration gradient generator for mechanical stimulation and drug delivery

Arash Yahyazadeh Shourabi ^a, Navid Kashaninejad ^{b,*}, Mohammad Said Saidi ^{a,**}^a Department of Mechanical Engineering, Sharif University of Technology, Tehran 11155, Iran^b Queensland Micro- and Nanotechnology Centre, Griffith University, Nathan Campus, 170 Kessels Road, Brisbane, QLD 4111, Australia

ARTICLE INFO

Article history:

Received 4 November 2020

Received in revised form

17 February 2021

Accepted 24 February 2021

Available online 3 March 2021

Keywords:

Concentration gradient generators

Fluid shear stress

Osmotic pressure gradient

Integrated microfluidic chip

Extracellular matrix

ABSTRACT

Mechanical stimuli, including fluid shear stress, osmotic pressure gradient, and extracellular matrix stiffness, significantly affect cellular interactions with drugs in biological structures. This paper introduces an integrated concentration gradient generator (CGG) capable of providing cell monolayers with these stimuli and demonstrates its design, fabrication, and quantification procedures. The proposed multi-layer chip consists of a CGG integrated with a membrane-based cell culture chamber (MCCC) and two bubble trappers for removal of micro-bubbles. The CGG provides cultured cells in the MCCC with four different concentrations of desirable inlet drug/chemical reagents. The MCCC is able to impose adjustable shear stresses, as well as osmotic pressure gradients on cell monolayers. The stiffness of the extracellular matrix (ECM) is also accommodating by utilizing a proper membrane in the MCCC. A numerical simulation based on the finite element method (FEM) is employed to design and optimize the integrated device, and then, the chip's performance is quantified using the experimental data. Finally, the biocompatibility of the proposed device is investigated by dynamic culturing of human lung cancer cells (A549 cell line) on the chip.

© 2021 The Authors. Publishing services by Elsevier B.V. on behalf of Vietnam National University, Hanoi. This is an open access article under the CC BY-NC-ND license (<http://creativecommons.org/licenses/by-nc-nd/4.0/>).

1. Introduction

From the mechanical point of view, biofluid shear stress, extracellular matrix (ECM) stiffness, and osmotic pressure gradient can significantly affect cells' behaviors and consequently, their cellular responses to drugs in biological systems. These parameters are among the key features that should be considered to better recapitulate *in vivo* features of cultured cells [1–4].

As a mechanical stimulus, shear stress is caused by blood flow, interstitial fluid flow, or lymphatic flow in biological systems [5]. Cells sense this mechanical signal and develop different biological responses, such as changes in morphology, orientation, polarization, adhesion, and differentiation. As such, signaling pathways and cell proliferation rate can be altered as a result of a mechanical stimulus while being treated with a drug [6–8]. ECM stiffness is

also a vital consideration in drug screening studies because it directly affects cell survival, proliferation, and signaling [1]. Osmotic pressure gradient arises from the difference in the concentration of solutes as well as the difference in the fluidic pressure between the luminal and the basolateral sides of cell-monolayers [8,9]. It causes the transportation of solutes and the fluid across the semi-permeable medium separating each side [9]. Osmotic pressure gradient directly affects cells' behaviors because of its role in cell volume regulation and mechanotransduction that elicit specific cellular responses [3].

Microfluidic perfusion platforms have recently gained widespread popularity in drug screening since they can provide cells with above-mentioned mechanical parameters [10,11]. These devices provide a micro-engineered cell culture model for high-resolution, cell-based assays and eliminate the massive gap between *in vivo* and *in vitro* conditions [12,13]. However, to be acceptable to the pharmaceutical industry, these systems need to be more user-friendly and automate test packages for real-time monitoring of drug responses and other bio-analyses in parallel [12,14]. In this regard, high-throughput drug screening using microfluidic chips has proved to be an efficient,

* Corresponding author.

** Corresponding author.

E-mail addresses: n.kashaninejad@griffith.edu.au (N. Kashaninejad), mssaidi@sharif.edu (M.S. Saidi).

Peer review under responsibility of Vietnam National University, Hanoi.

reliable method of *in vitro* biological tests that facilitates parallel measurement of several parameters on cells or other biological elements in a low-cost and time-saving manner [15,16]. The primary approach in turning microfluidic systems into high-throughput platforms is to develop engineered, integrated microfluidic chips [17].

CGGs are microfluidic devices that generate several concentrations of an input drug or a chemical reagent at their outlets for drug-screening, cell growth, chemotaxis, and other biological processes [18–22]. These systems are considered as one of the most required elements in organ-on-chip and cell-based screening platforms [19]. CGGs could be subcategorized into diffusion-based, pressure balance, T-junction, hydrogels, and tree-like CGGs [19]. Utilizing laminar flow properties, tree-like CGGs generate more stable and continuous gradients and have been used in most drug screening applications [19,20]. The main idea of designing an integrated drug screening microchip is to integrate a CGG with a cell culture chamber on one single chip to function in a series automatically [21]. Numerous studies have developed such microchips that integrate various subcategories of CGGs with different types of cell/tissue culture chambers [15,17,23–33]. Park et al. designed and quantified a perfusion cell culturing platform integrated with a CGG, which provided separated culturing chambers with different concentrations of an input reagent simultaneously [31]. The microfluidic chip proposed by Sun et al. is a drug combinatorial CGG integrated with several, separate culturing side-chambers [26]. In another study, Lim presented a CGG integrated with spheroid culturing chambers for 3D cell aggregates studies [34]. However, in all of these designs, important *in vivo* factors for cell monolayers such as adjustable shear stress, osmotic pressure gradient, and ECM stiffness were absent.

To address the limitations mentioned above, we took a step forward towards designing an Integrated CGG capable of providing cultured cells with three primary mechanical stimuli. These mechanical stimuli include precise, diverse, and manageable shear stresses, osmotic pressure gradients, and ECM stiffnesses.

In this work, we demonstrate a multipurpose, membrane-based microfluidic CGG with potential applications in drug-screening, drug delivery, and personalized medicine. Consisting of bubble trappers, a culture medium reservoir, a tree-like CGG, and a membrane-based cell culture chamber (MCCC), all integrated on one single chip, the device is able to facilitate rapid, high-content studies on cell monolayers. The chip is capable of imposing osmotic pressure gradients on cells since the fluid in its bottom layers' reservoir, and the flow in the upper MCCC's layer plays the role of basolateral fluid and the luminal flow for cells respectively. Cell-monolayers could be exposed to different, precise magnitudes of shear stress while the CGG maintains its function under different flow rates, and bubble trappers remove disturbance making micro-bubbles from the flow before its introduction to the CGG. Also, various reagents' concentrations could be tested on cells simultaneously owing to the CGG. In addition to that, the user can follow the same illustrated procedure in this manuscript with other commercial or non-commercial membranes to provide cells with their required extracellular matrix stiffness. Epithelial or endothelial cells of kidney, lung, liver, and other organs with similar culturing conditions could be cultured on the chip, where the *in vivo*-like conditions of cells can be provided by merely adjusting the required shear stress (through adjusting the syringe pump's flow rate), ECM stiffness (by assembling layers with a proper membrane), and the osmotic pressure gradient (simply by varying the concentrations of solutes in the bottom layer's reservoir) by the operator. In the following sections, the performance of bubble

trappers, the CGG, and the ability of the MCCC in dynamic cell-monolayer culturing will be shown both numerically and experimentally.

2. Working principle and model description

Fig. 1 demonstrates the schematic of the integrated microfluidic package. The device is a two PDMS-layer microfluidic chip with a porous membrane sandwiched in between. The bottom layer consists of a culture medium reservoir. On the upper layer, there are two bubble trappers, a concentration gradient generator (CGG), and a membrane-based cell culturing chamber (MCCC) that mimics the *in vivo*-like environment in which cells are exposed to shear stress and osmotic pressure gradient (Fig. 1(d)). The upper layer includes two inlets for the drug and its diluter. There are two other ports in the vicinity of the MCCC to fill or evacuate the bottom layer's quasi-static reservoir. The flow in upper layer channels first reaches the bubble trappers, where the buoyancy force removes bubbles and traps them in the cylindrical bubble reservoirs, each 4 mm in diameter and 3 mm in height. These bubbles usually form in the system because of the connections of silicon tubes to the chip and the remaining micro-bubbles in syringes.

It is crucial to remove bubbles prior to their entrance into the main system to guarantee the CGG's performance, better on-chip cell viability, and to control the precise magnitude of fluid shear stress on cells. It was reported that unwanted bubbles could increase the shear stress on cells by one order of magnitude [31,35,36]. After the bubble-removing step, the free-bubble fluid flows through the CGG, consisting of micro-channels 200 μm in width and 400 μm in height. Finally, four different concentrations of the injected drug would form a four-drug zone in the MCCC (one control section and three drug sections). Subsequently, cultured cells will be treated with these concentrations in the culture chamber. The proposed integrated microfluidic chip benefits from novel and unique advantages. It is designed to be a universal platform capable of culturing cell monolayers on an adjustable porous substrate and exposing them to various shear stresses in the range of $0 - 4 \text{ dyn/cm}^2$ (which covers the range used in most organ-on-chip or other cell-based platforms [36–40]), osmotic pressure gradients, and diverse concentrations of drugs with a diffusion coefficient of higher than $5 \times 10^{-10} \text{ m}^2/\text{s}$ (which is a typical value for many drugs and chemical reagents [19]). Applying microscope and image processing techniques, drug metabolism and cytotoxicity, cell permeability to various substances, and cell morphology due to different fluidic conditions could be analyzed all in parallel on this chip rapidly and accurately as some of its potential applications in on-chip bioassays. The proposed chip would also lead to consuming fewer materials and reagents than conventional methods which proved not to be efficient enough, especially in multi-toxicity bioassays [28]. Also, there is no need to fabricate several chips and couple them with CGG chips, which causes several errors in experiments and seems not to be high-throughput practically.

3. Numerical simulation and optimization

Considering microfabrication limitations and integration of the chip, it was crucial to perform a theoretical simulation on the concept prior to any experimental practices. The main challenge in designing integrated chips is the interconnection between all sections of the system, so in designing and optimizing each part of the chip, its effects on other parts of the system should be taken into account.

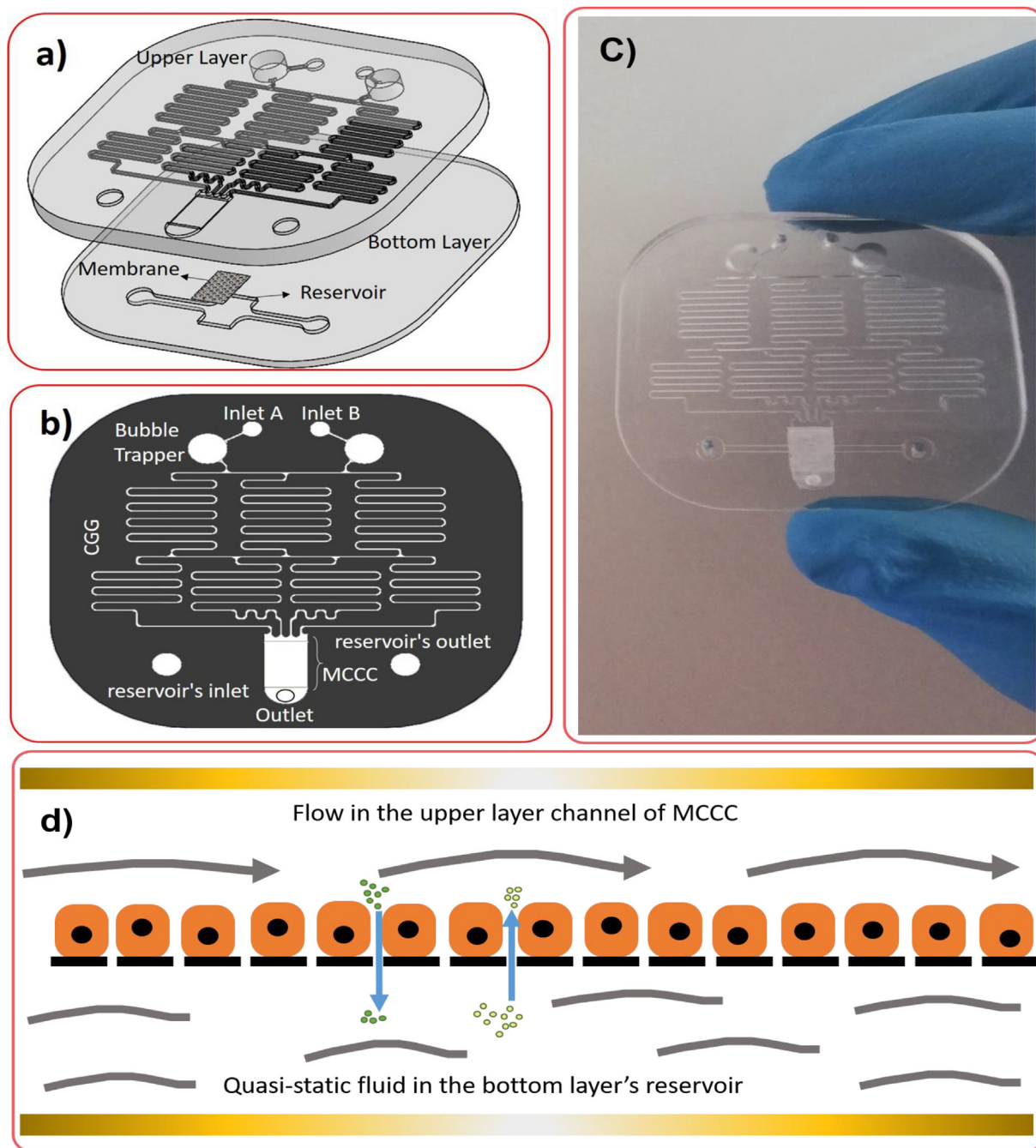


Fig. 1. a) Schematic exploded view of the designed microfluidic chip. b) Upper layer contents in detail. c) The final assembled chip. d) The cell culture chamber which mimics *in vivo* conditions to impose controlled shear stress and osmotic pressure gradient on cell monolayers. FSS is caused by the flow of fluid in the luminal channel of the MCCC, while osmotic pressure gradient is the result of both pressure and concentration differences between the luminal and the basolateral sides. This gradient is responsible for the transportation of water and solutes across the membrane, which is shown here schematically.

All of the governing equations were solved utilizing the finite element method (FEM) and structured mesh elements in COMSOL Multiphysics 5.3 to design and optimize the integrated chip. The FEM has been proved to be a reliable tool in the microfluidics area [41]. Optimization procedures for the CGG include channel sizing, finding mixing lengths, and locating T-junctions to guarantee its mixing performance at flow rates up to $124 \frac{\mu\text{L}}{\text{min}}$ for various ranges of drugs with diffusion coefficients higher than $5 \times 10^{-10} \text{ m}^2/\text{s}$. For the cell culture chamber, the goal was to find the cell culture chamber's height and width in order to ensure precise and

uniform shear stress on all cells in width and length of the chamber, having sufficient cell population, and finding out if the minimum required amount of oxygen and glucose reach to all cells. In addition, it was necessary to prevent mixing in the cell culture chamber in order to generate four equal-sized, distinct drug concentration zones.

Moreover, the bubble trapper was designed and simulated. The bubble trapper reservoir's diameter and height were found in a way so that the buoyancy force could overcome the flow's momentum carrying the bubbles and removes and stores all bubbles

Table 1
Summary of the simulated equations.

Part	Physical equations	Consideration
Bubble trapper	Navier–Stokes – Continuity- Two-phase flow (level-set)	To obtain the bubble reservoir's diameter and height
CGG	Navier–Stokes – Continuity- Transport of concentration	To obtain channels' sizes, T-junctions' locations, and the mixing length
MCCC	Navier–Stokes – Continuity- Transport of concentration Michaelis–Menten kinetics - Kedem–Katchalsky equatio	To obtain the chamber's width and height

in the cylindrical reservoir. Another criterion is to have sufficient capacity for bubble trappers in order to provide the chip with a bubble-free flow during culturing. Trapped bubbles finally leave the system through gas permeable PDMS walls during its operation [42].

3.1. Theories and relationships

Laminar flow equations, consisting of continuity and Navier–Stokes equations, govern the flow's field in the whole system which can be expressed respectively as [43]:

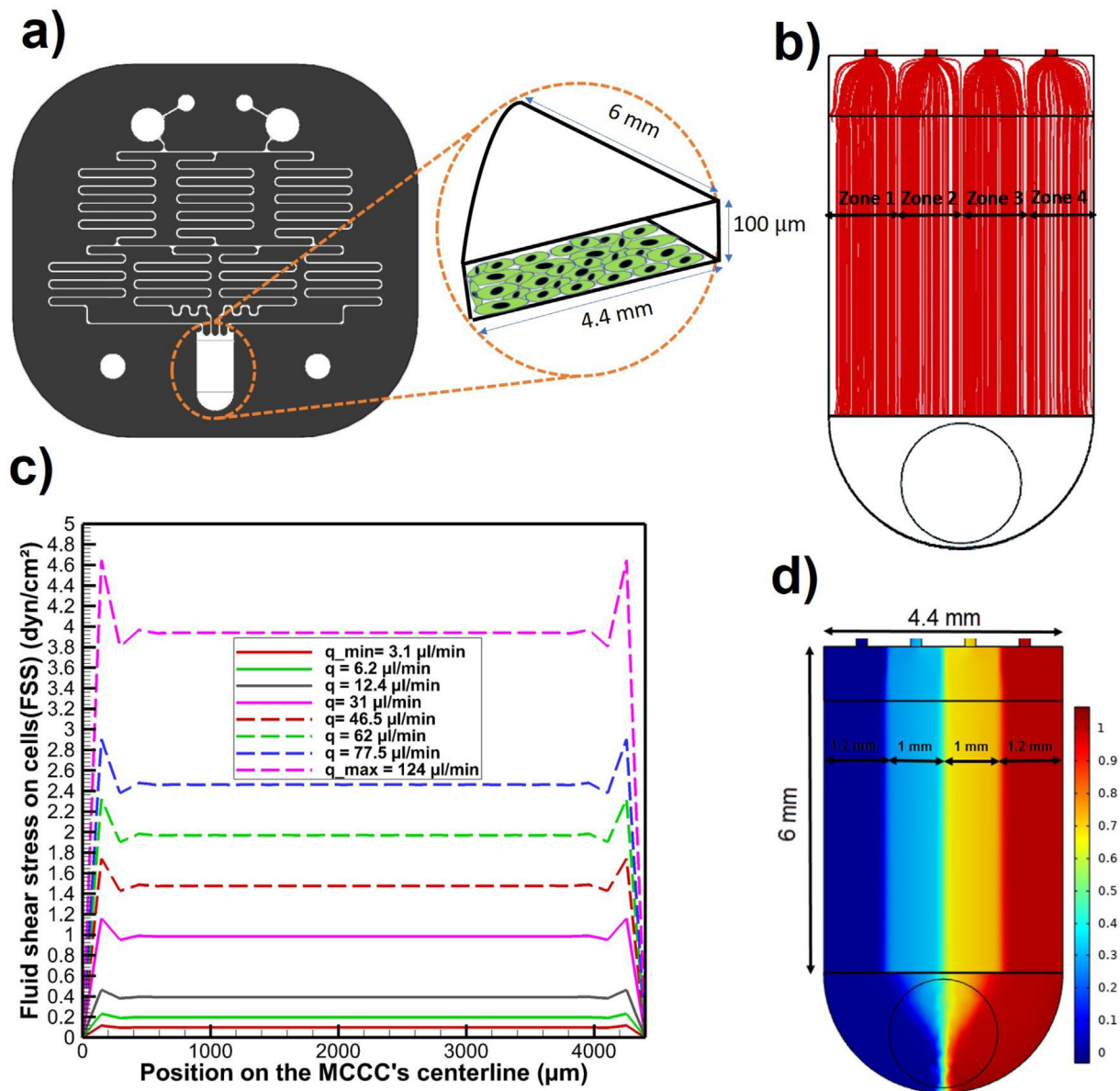


Fig. 2. a) Luminal section of the MCCC's geometry and its dimensions. The bottom layer's reservoir (basolateral section) has a similar width and length to the luminal side, but the depth was chosen to be 500µm for better microscopy analysis. b) Uniform streamlines of the flow on cells. Because of the engineering of the chip and the properties of laminar flow, four distinguished fluidic zones are formed regularly in the MCCC which eliminates the necessity of using any physical parts to separate zones from each other. c) Distribution of FSS on cells cultured in the MCCC at various operational flow rates. The 200 µm offset at each side of the MCCC is enough to cut off cells receiving non-uniform fluid shear stresses from the statistical population. This non-uniformity is the reason for the intense gradient in the velocity profile near walls. d) Four distinct drug concentration zones formed in the MCCC. The MCCC was designed in a way to inhibit mixing in the MCCC and to have negligible boundary layers that separate zones from each other.

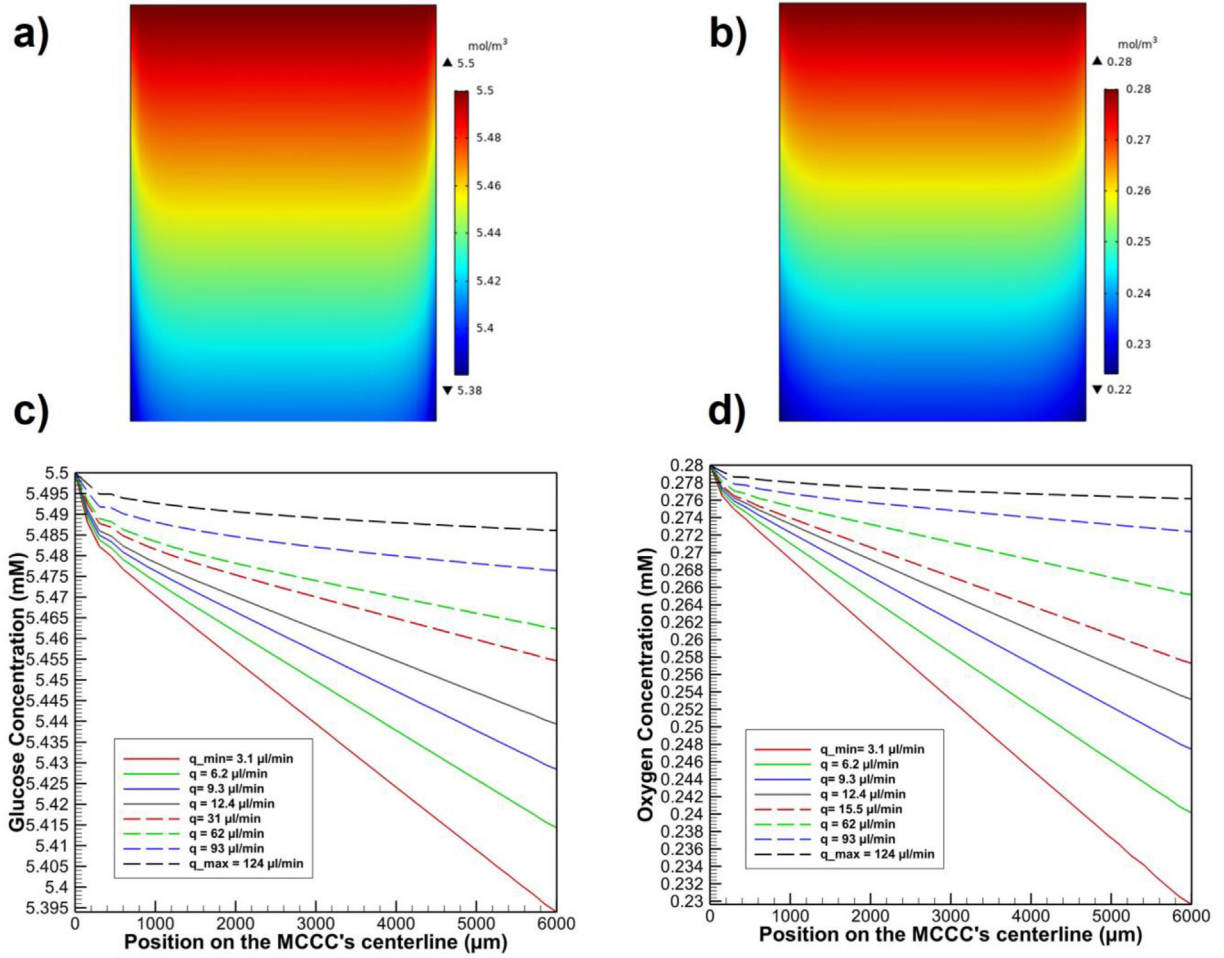


Fig. 3. a) and b) Glucose and oxygen concentration distributions in the MCCC for the flow rate of $3.1 \frac{\mu\text{l}}{\text{min}}$ which is the critical flow rate for cell viability on the chip. Cells located downstream of the chamber receive fewer amounts of nutrition than those located upstream of the flow, but still, they receive sufficient glucose and oxygen concentrations. Adjacent to the wall, where is the $200 \mu\text{m}$ non-uniform FSS region, cells receive the least amount of nutrition because of the physics of laminar flow's boundary layer there. c) and d) Glucose and oxygen concentration distributions on the longitudinal midline of the MCCC. All cells receive a sufficient amount of nutrients at all of the chip's operational flow rates. The higher the flow rate, the more uniformity is observed in the distribution of nutrition alongside the chip; thus, cells would be in similar nutritional states at higher flow rates.

$$\vec{\nabla} \cdot \vec{V} = 0 \quad (1) \quad D_k (\nabla^2 C_k) - \vec{V} \cdot \nabla C_k = 0; k = 1, 2, 3 \quad (4)$$

$$\rho (\vec{V} \cdot \vec{\nabla}) \vec{V} = -\vec{\nabla} p + \mu (\nabla^2 \vec{V}) \quad (2)$$

where \vec{V} is the velocity vector, p is the pressure, μ is the dynamic viscosity, and ρ is the density. By solving Eqs. (1) and (2) in the computational domain, flow's field in all CGG's channels and bubble traps, system's total pressure drop, shear stress on cells, and flow's hydrodynamic condition in the cell culture chamber are determined. To evaluate the accuracy of numerical results, values of shear stress in the MCCC were compared to those predicted by the analytical relation below [2]:

$$\tau = 6\mu Q / bh^2 \quad (3)$$

where Q is the total flow rate in the cell culture chamber, b and h are the chamber's width and height, respectively. Next, the concentration distribution of drug, oxygen, and glucose could be obtained by coupling the laminar flow equations to the equation of transport of the dilute species as follows [25]:

where D_k and C_1 are the drug or chemical reagent's diffusion coefficient and concentration, respectively. Also, C_2 and C_3 are oxygen and glucose concentrations, respectively. In the cell culture chamber, considering the cell monolayer's metabolism and its imposition to osmotic pressure gradient, Michaelis–Menten kinetics was utilized for active transport phenomena simulation, and the passive transport was modeled using Kedem–Katchalsky equations in order to find water and solute fluxes through cell monolayer as [44]:

$$J_v^u = h_v^u \left(\sum_k RT (C_k^u - C_k^d) \sigma_k^u + P^d - P^u \right); k = 3, 4 \quad (5)$$

$$J_k^u = J_v^u (1 - \sigma_k^u) \frac{(C_k^u + C_k^d)}{2} + h_k^u (C_k^u - C_k^d) + \frac{V_{max,k}^u C_k^u}{K_{m,k}^u + C_k^u}; k = 3, 4 \quad (6)$$

where J_v^u is the water flux, J_k^u is the solute flux, h_v^u is the hydraulic permeability coefficient of the wall, P^d is the hydrostatic pressure in

the bottom layer's reservoir, P^u is the hydrostatic pressure in the upper channel of the cell culture chamber, σ_k^u is the Staverman reflection coefficient, h_k^u is the permeability of k -th specie through the wall, $K_{m,k}^u$ is the Michaelis–Menten constant, and $V_{max,k}^u$ is the maximum rate of transport.

The bubble trapping process in bubble trapper's reservoirs was simulated as a two-phase flow model through the level-set method, in which the interface of two incompressible fluids is traced by the time-dependent convection equation [44]:

$$\frac{\partial \phi}{\partial t} + \vec{V} \cdot \nabla \phi = 0 \quad (7)$$

where ϕ is an implicit function, called the level set function, which defines the interface of the two discrete phases. All designing considerations for the simulation are summarized in Table 1.

4. Materials and methods

4.1. Fabrication of the microfluidic device

For each layer, a polymethyl methacrylate (PMMA) positive master mold (47.4 mm × 43.65 mm) was fabricated by micro-milling method (Roland MDX-40a, Japan). The upper layer's mold contains two bubble trappers (2 mm radius and 3 mm high), a CGG (microchannels with 200 μm wide and 400 μm high), an MCCC (4.4 mm wide, 6 mm long and 100 μm high considering the membrane's surface as the origin) and the inlet/outlet ports. The bottom layer's mold also consists of the culture medium reservoir (4.4 mm wide, 6 mm long and 500 μm deep). Then, a mixture of PDMS and curing agent (SYLGARD® 184 SILICONE ELASTOMER KIT, Sigma–Aldrich, USA) with a weight ratio of 10:1 was cast on molds. PDMS was cured in an oven at 75 °C for 2 h after degassing for 20 min in a vacuum chamber. Whatman® cellulose-fiber porous membrane (pore size 2.5 μm) was used as the MCCC's substrate of on-chip cell culturing.

Eventually, both of the PDMS layers and the porous membrane were all bonded irreversibly using the plasma cleaning technique. For aligning layers in the bonding process, we utilized two guide

pins (diameter: 2 mm) fixed in the bottom layer's reservoir's inlet/outlet port on the upper layer. For silicon tubes connection (outer diameter: 2 mm, inner diameter: 600 μm) to the syringe pump, upper layer's ports were drilled by a 1.5 mm biopsy punch. The PDMS wall thickness above bubble trappers' ceilings was chosen to be 500 μm to improve gas permeability and facilitate microscopy and imaging.

4.2. Cells and reagents

Human lung cancer cells (A549) were purchased from Pasture general cell collection (Tehran, Iran). The culture medium was based on high glucose DMEM (Dulbecco's Modified Eagle Medium–Gibco, USA) supplemented with 10% fetal bovine serum (Gibco, USA) and 1% penicillin-streptomycin. For preparation of cell suspension and static cell-related tests, cells were cultured in T-25 flasks (SPL life sciences, South Korea) and placed in an incubator adjusted for 37 °C and 5% CO₂. The media was changed every two days, and for about 85% of confluence, passaging was performed. The final cell suspension was prepared by diluting of $5 \times 10^5 \frac{\text{cells}}{\text{mL}}$ in DMEM. Cell counting was performed by utilizing an HGB Neubauer counting chamber (HGB, Germany) and Trypan Blue Solution (ThermoFisher Scientific, Catalog number: 15250061). Visualizing the cell monolayer was performed via live-cell staining technique with the aid of Acridine Orange (ThermoFisher Scientific, Invitrogen™, Catalog number: A1301) as the staining kit.

4.3. Preparation of the microfluidic chip for cell seeding

To prepare the microchip for bioassays, firstly it was sterilized in an autoclave and then exposed to UV light for 30 min. Then all channels and interior parts were washed using 70%_{v/v} ethyl alcohol for 15 min. Finally, to remove any remaining alcohol in channels, PBS buffer was perfused through channels several times. In all stages, we used a precise syringe pump (ET- SP-V1, SATEECO Co., Iran). The cellulose-fiber membrane was also treated with plasma and coated with gelatin prior to cell culture.

Table 2
Numerical values of the simulation parameters.

Parameter	Value	Reference
D_{Oxygen}	$2.6 \times 10^{-5} \frac{\text{cm}^2}{\text{s}}$	[24]
D_{Glucose}	$9.25 \times 10^{-6} \frac{\text{cm}^2}{\text{s}}$	[24]
$V_{max, \text{Oxygen}}^u$	$7.37 \times 10^{-17} \frac{\text{mol}}{\text{s cell}}$	[24]
$V_{max, \text{Glucose}}^u$	$0.39 \times 10^{-16} \frac{\text{s}}{\text{cell mol}}$	[24]
$K_{m, \text{Oxygen}}^u$	$4.63 \times 10^{-6} \frac{\text{mol}}{\text{L}}$	[24]
$K_{m, \text{Glucose}}^u$	$4.00 \times 10^{-5} \frac{\text{mol}}{\text{L}}$	[24]
h_v^u	$5 \times 10^{-12} \frac{\text{m}^3}{\text{N} \times \text{s}}$	[45]
σ_{Oxygen}^u	0.79	[46]
$\sigma_{\text{Glucose}}^u$	6.5×10^{-2}	[45]
h_{Oxygen}^u	$56.1 \times 10^{-10} \frac{\text{mol}}{\text{N} \times \text{s}}$	Estimated from [45]
h_{Glucose}^u	$9.35 \times 10^{-10} \frac{\text{mol}}{\text{N} \times \text{s}}$	[45]
Concentration of oxygen in DMEM	$0.28 \frac{\text{mol}}{\text{m}^3}$	[38]
Concentration of glucose in DMEM	$5.5 \frac{\text{mol}}{\text{m}^3}$	[38]

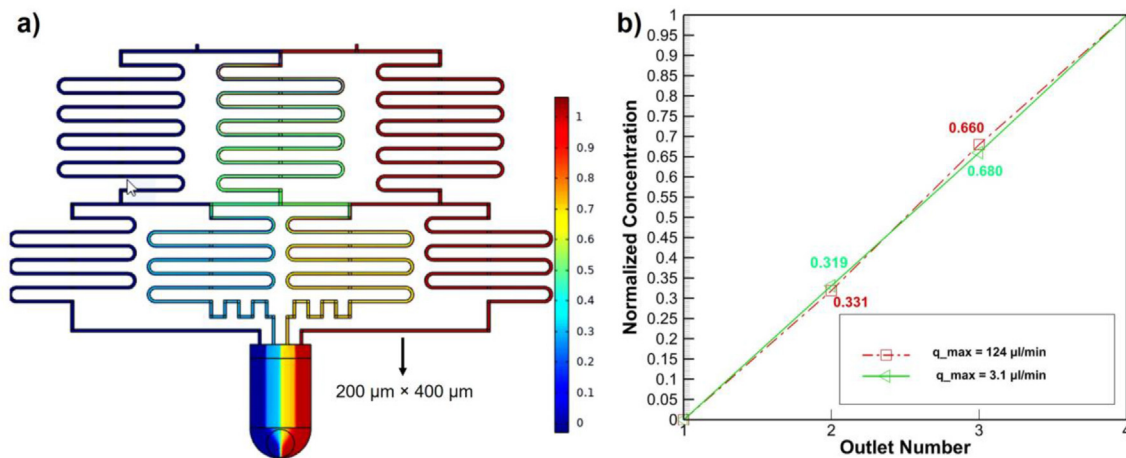


Fig. 4. a) Graphical view of the drug dilution in the CGG (normalized). b) Performance of the CGG at each outlet ($q_{\max} = 124 \frac{\mu\text{l}}{\text{min}}$, $q_{\min} = 3.1 \frac{\mu\text{l}}{\text{min}}$).

4.4. Fluorescence microscopy

In the present work, all experimental tests were completed at least in triplicate independently. Observation of all assessments and experimental tests was carried out using an inverted fluorescence microscope (Labomed TCM400, CA, USA) coupled with a CCD camera (MD-30, Mshot Co., China).

5. Results and discussion

5.1. Simulation results

Fig. 2 demonstrates simulation results and the optimized geometrical features of the cell culture chamber. In Fig. 2(a), the dimensions of the upper layer's channel of the cell culture chamber are shown. The step-like cross-section at the chamber's inlet provides more uniform flow and shear stress on all cells at every location of the chamber, which is illustrated more by plotting streamlines in Fig. 2(b). As shown in Fig. 2(c), various

magnitudes of FSS are attainable by adjusting the proper infusion rate at inlets by the user. Each of four drug concentration zones in the chamber was designed to be 1 mm in width, like former on-chip works [8], and 6 mm in length [10]. However, a 0.2 mm offset was considered from both sides because of the non-uniformity of the shear stress near walls, as illustrated in Fig. 2(d). So, cells in this limited area will be eliminated from the statistical population in future analyzing affairs since they are experiencing different culturing conditions, with respect to the cells that are out of this margin.

Figs. 2(b) and 3(a) describe glucose and oxygen concentration distribution on cells for an inlet flow rate of $3.1 \frac{\mu\text{l}}{\text{min}}$ at each of the inlets (shear stress equals to $0.1 \frac{\text{dyn}}{\text{cm}^2}$), which warrants avoiding hypoxia and anoxia zones formation in the MCCC for this and higher flow rates. Considering the universality of the chip, to solve Eqs. (4)–(6), cancerous cells' parameters were chosen from the literature. Details are reported in Table 2.

Values of oxygen and glucose concentrations on the MCCC's centerline for various flow rates are plotted in Fig. 3(c), (d). The

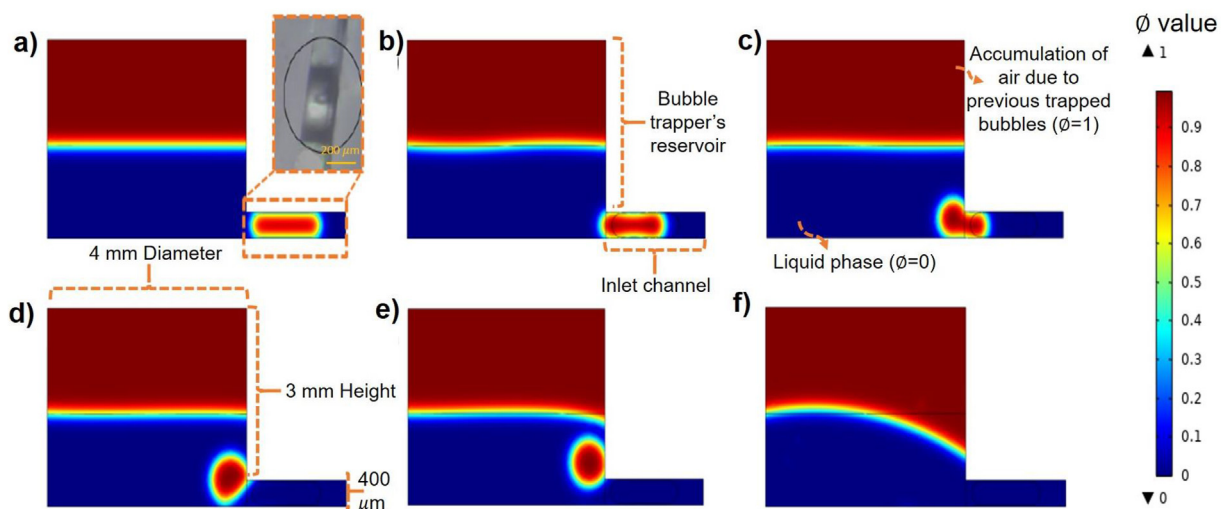


Fig. 5. Tracing the bubble in the trapping process at six different time stages (a to f) for $q = 124 \frac{\mu\text{l}}{\text{min}}$. The bubble is introduced to the system from the inlet and travels through the channel with a constant morphology (stage a). As soon as the bubble reaches the trapper's reservoir, its morphology starts to change (stage b). Once the bubble starts to enter the reservoir, the buoyancy force pushes the bubble upward because of the difference in the density of water and of the air inside the bubble (stage c). Then, the bubble exits the microchannel completely and starts to form a sphere (stage d). The formed spherical bubble travels upward due to the buoyancy force (stage e). Finally, the bubble joins other bubbles that have been previously trapped and stored in the reservoir's upper region (stage f).

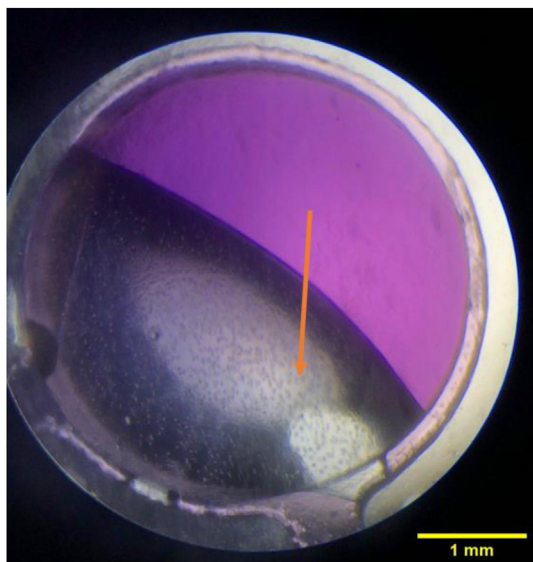


Fig. 6. Microscopic image of the bubble trapper while operating. Violet-colored water was injected into the chip for better visualization of the bubble trapping process under the microscope.

results obtained prove the point that none of the cells at any locations of the monolayer would ever suffer from lack of nutrients for all of the chip's operational flow rates. By increasing the syringe pump's infusion rate, the mass of nutrients reaching the MCCC would rise. For this reason, the flow rate of $3.1 \frac{\mu\text{L}}{\text{min}}$ is the chip's critical operational flow rate and was chosen to be the criterion of this section's simulations.

Fig. 4(a) demonstrates the dimensions and the performance of the engineered CGG. Channels' sizes and the mixing length were designed to have four outlet concentrations with less than 5% deviation from the ideal mixing state (0, 33, 66, and 100%). Also, the CGG must maintain its performance under various inlet flow rates (Fig. 4(b)). To balance the pressure drop between all of four CGG's

outlets, zigzag-shaped dampers were designed for outlet number two and outlet number three.

The bubble trapper was designed to maintain its reliable performance at high flow rates ($124 \frac{\mu\text{L}}{\text{min}}$ or equivalently 4 dyn/cm^2 of the shear stress in the MCCC). This designing criterion ensures us of the trappers' capability at lower flow rates. Because the lower is the flow rate of the fluid, the lower is its momentum, so that the buoyancy force has more time to push the bubbles upward out of the mainstream of the flow. The bubble's shape and dimensions for simulation were found from some simple observations of bubbles in microfluidic chips with similar CGG's channels and experimental setups. Details of the simulation are expressed in Fig. 5 in which the bubble's behavior in the bubble trapper's reservoir and the inlet channel connected to it is observable. In the simulation, it is assumed that the chip was already working steadily before the introduction of this bubble into the system, and some bubbles had been previously trapped and stored in the reservoir and formed a gaseous phase in the upper region of the reservoir. The red color represents the region that is occupied with the gaseous phase ($\phi = 1$, or air) while the liquid phase is shown in blue ($\phi = 0$, or culture media). The narrow gradient from red to blue is also the interface of the two phases.

5.2. Device characterization and quantification

5.2.1. Bubble trapper

First of all, the performance of the proposed bubble trapper was examined. During experimental tests, it was observed that periodic connecting and disconnecting the silicon tubes from syringes (during the process of refilling syringes) was the primary source of bubble formation. For better visualization, violet-colored water was used at inlets, as shown in Fig. 6. Bubbles were introduced to the system by connecting and disconnecting silicon tubes carefully from syringes periodically to produce micro-bubbles in the system. The flow rate was set on $124 \mu\text{L}/\text{min}$. The bubble-free MCCC and trapped bubbles proved that designed trappers could remove all the bubbles for cell culturing of about two whole days.

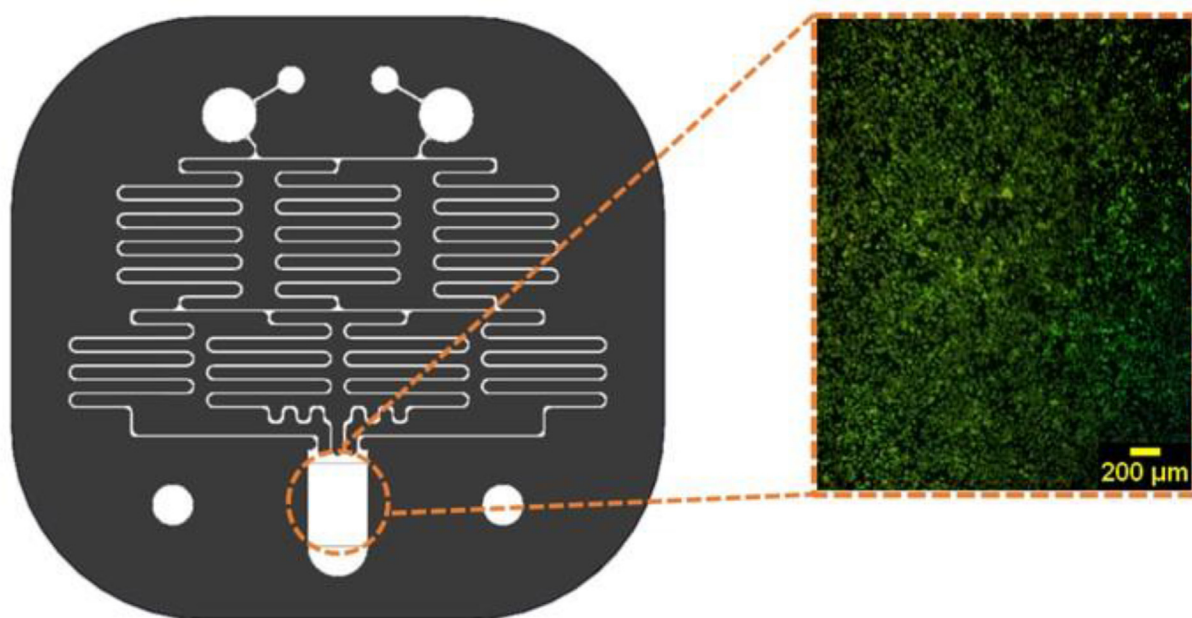


Fig. 7. Fluorescence image of the cell monolayer stained with acridine orange to check the uniformity. A layer of live cells approximately has covered the area completely.

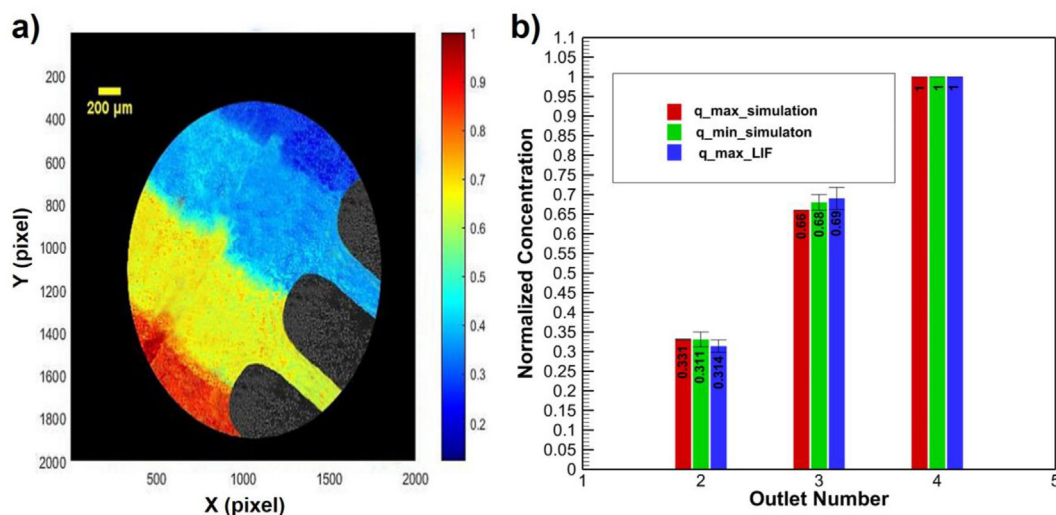


Fig. 8. a) Normalized concentration of Rhodamine B. The enhanced contour obtained from processing the LIF images in MATLAB. (flowrate = $124 \frac{\mu\text{l}}{\text{min}}$). b) Comparison between simulation results and experimental results at high flow rates. $q_{\text{min_simulation}}$ represents the minimum flow rate of the simulation ($3.1 \frac{\mu\text{l}}{\text{min}}$), $q_{\text{max_simulation}}$ represents the maximum flow rate of the simulation ($124 \frac{\mu\text{l}}{\text{min}}$) and $q_{\text{max_LIF}}$ is the highest flow rate at which the LIF experiment was conducted ($124 \frac{\mu\text{l}}{\text{min}}$). Error bars represent the deviation of each bar from theoretical, normalized concentrations (0, 0.33, 0.66, and 1).

5.2.2. Membrane-based cell culture chamber (MCCC)

Secondly, the biocompatibility of the chip for both static and dynamic cell culture was assessed. For static cell culture, the cell suspension was injected into the chip from the outlet port. Then, the chip was incubated at 37°C with 5% CO_2 for cell attachment. Next, the upper layer channel of the MCCC was filled with culture medium, and a slight flow of $0.1 \frac{\mu\text{l}}{\text{min}}$ was applied to the bottom layer's reservoir to perfuse an abundant amount of culture media to cells. In this way, cells are cultured in a shear-free environment. The chip was then placed in a CO_2 incubator until cells were grown abundantly to form a confluent monolayer after two days. For dynamic cell culturing on the chip, right after the static culturing reached a confluence level of 85%, and cells were incubated for two days, a continuous media flow at the rate of $3.1 \frac{\mu\text{l}}{\text{min}}$ (in the upper layer channel) was imposed upon cells. This flow rate is the critical flow rate for cellular survival and was obtained from numerical simulations. The bottom layer's channel was filled with

culture medium and maintained in quasi-static mode during the process of dynamic culturing. After 24 h of dynamic culturing, the membrane was cut carefully out of the chip using a sharp surgical blade. After that, the membrane was rinsed by PBS buffer, and then cells were trypsinized and collected. Then, the trypan-blue assay was conducted on them. With this approach, unwanted cells that were seeded in channels and tubes are not counted, and the acquired number will be purely due to the cells in the MCCC. After each cell seeding, almost 48,000 live cells adhered to the membrane of the MCCC. Results show that the chip possesses a high cell viability rate (95%). To check the uniformity of the cell monolayer on the chip, the following staining procedure was performed on the cells cultured on the MCCC's upper channel. After the dynamic culturing was completed, utilizing the syringe pump on the suction mode, we filled the MCCC's upper channel with 1 mg/ml acridine orange and incubated the chip for 20 min. Then, immediately after incubation, cells were washed with PBS. Then, the MCCC part was

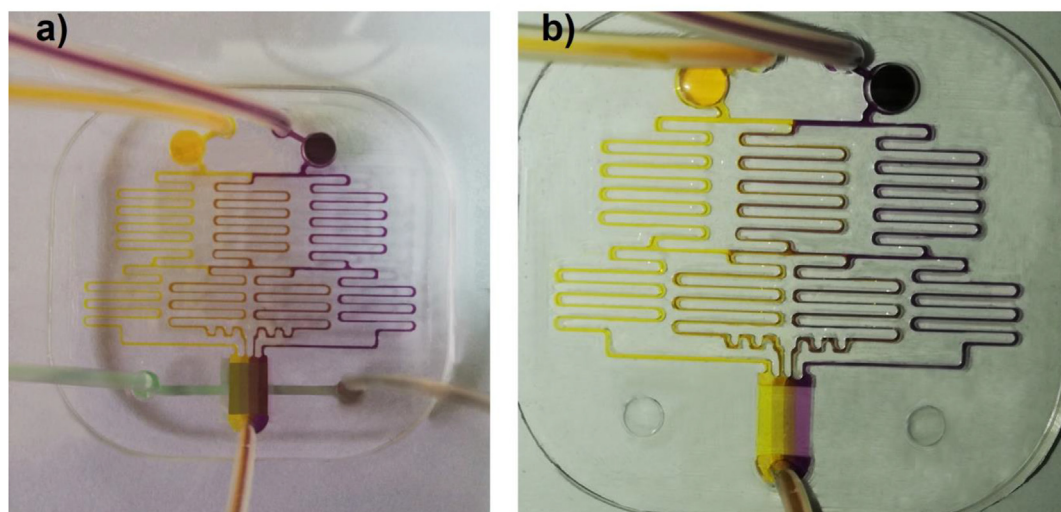


Fig. 9. CGG's performance visualization by introducing violet-colored water and golden yellow-colored water at inlets ($q = 124 \frac{\mu\text{l}}{\text{min}}$). a) Single-layer chip without integrating the membrane for better visualization. b) Two-layer chip integrated with a treated membrane.

excited with a 502 nm laser, and finally, implementing a 525 nm filter, observations were made using an inverted fluorescence microscope. Fig. 7 shows the fluorescence image of the stained cells, which proves the uniformity of the cell monolayer. Also, cell density was calculated to be $182,000 \frac{\text{cells}}{\text{cm}^2}$ which is similar to that obtained from culturing A549 confluent cell monolayers on T25 flasks.

5.2.3. Concentration gradient generator (CGG)

The CGG's efficiency was examined experimentally by applying LIF (Laser Induced Fluorescent) technique. Rhodamine B (diffusion coefficient = $4.2 \times 10^{-10} \frac{\text{m}^2}{\text{s}}$ which is lower than the diffusion coefficient that was used for simulation, excitation wavelength = 561 nm) [47] was injected into one inlet, and pure distilled water was injected into the other one. The flow rate was chosen to be $124 \frac{\mu\text{l}}{\text{min}}$ which is the maximum desired flow rate of the chip to function. For better imaging, the concentration of Rhodamine B was chosen to be 1.67×10^{-4} mol of Rhodamine B/1 lit of pure water. Finally, three images with twenty-minute intervals were snapped and then processed using a LIF code in MATLAB after averaging intensities of them. The required time for a stable gradient at CGG's outputs was also found to be only five minutes. LIF results show that the CGG operates stably and deviation from the ideal simulated concentrations are less than 5% (Fig. 8).

For better visualization of the CGG's performance, in Fig. 9, violet-colored water and golden yellow-colored water were introduced to the chip. Here, just for visualization purposes, we brushed the membrane with the PDMS/reagent mixture (1:10) and baked it for 10 min in the oven (75 °C). In this way, the membrane became more transparent and also easier to handle, so the visualization enhanced greatly. In addition to visualization, the colored-water technique is beneficial to observe whether the bonding or connections have any leakages or not.

6. Conclusion

The design, fabrication, and quantification of an integrated, high-throughput, membrane-based microfluidic CGG were presented. The CGG facilitates the gradient generation of a vast range of drugs and chemical reagents for high-content cell-monolayer-based assays, while the MCCC mimics an *in vivo* microenvironment for cells by imposing FSS and osmotic pressure gradient simultaneously upon them. By integrating bubble trappers into the platform, the stable concentration gradient generation and bubble-free cell culturing were provided. First, we discussed the vital importance of osmotic pressure gradient, shear stress, drug concentration, and ECM stiffness in cell culturing and related bioassays. Second, we presented our novel chip and simulated it numerically via a FEM approach in COMSOL Multiphysics for an optimum and reliable design. It was observed that a 0.2 mm margin should be considered from each of MCCC's sidewalls to cut-off cells that are receiving undesirable values of FSS. Additionally, it was shown that by increasing the flow rate, glucose and oxygen distribute more evenly in microfluidic cell culture chambers. Through the next step, chip fabrication and cell-based practices were defined in details. After that, the chip performance and the simulation were evaluated experimentally in three sections. We used Rhodamine B and image processing techniques (LIF) for CGG's performance quantification. Probable bubbles' sizes were observed experimentally, and the capacity of bubble trappers to remove bubbles for bubble-free culturing was achieved. Most importantly, the chip was tested for high cell viability in both static and dynamic cell culturing conditions.

To sum up, the chip proved to be an easy-to-fabricate, low-cost, and high-throughput CGG with applications in organ-on-chip, drug

screening, and drug delivery studies. The chip and its method could be utilized for different drugs and cell types. This approach reduces time and material consumption in comparison to macro-scale, conventional methods. Exposing cells to different osmotic pressure gradients, different drug concentrations, and diverse values of shear stress simultaneously, in addition to the adjustability of ECM stiffness (regarding the integrated membrane's properties), turn this chip into a universal package for cell-based bioassays and pave the way for novel experiments and assessments in cytotoxicity research areas. For future works, our group aims to investigate the toxicity effect of different concentrations of Cisplatin on renal cells utilizing the proposed chip.

Declaration of competing interest

The authors declare that they have no known competing financial interests or personal relationships that could have appeared to influence the work reported in this paper.

References

- [1] R.G. Wells, The role of matrix stiffness in regulating cell behavior, *Hepatology* 47 (2008) 1394–1400, <https://doi.org/10.1002/hep.22193>.
- [2] S. Feng, S. Mao, Q. Zhang, W. Li, J.-M. Lin, Online analysis of drug toxicity to cells with shear stress on an integrated microfluidic chip, *ACS Sens.* 4 (2019) 521–527, <https://doi.org/10.1021/acssensors.8b01696>.
- [3] M. Wang, Y. Yang, L. Han, F. Xu, F. Li, Cell mechanical microenvironment for cell volume regulation, *J. Cell. Physiol.* 235 (2020) 4070–4081, <https://doi.org/10.1002/jcp.29341>.
- [4] S. Yadav, N. Kashaninejad, N.-T. Nguyen, RhoA and Rac1 in liver cancer cells: induction of overexpression using mechanical stimulation, *Micromachines* 11 (2020) 729, <https://doi.org/10.3390/mi11080729>.
- [5] S. Shurbaji, G.G. Anlar, E.A. Hussein, A. Elzatahry, H. C Yalcin, Effect of flow-induced shear stress in nanomaterial uptake by cells: focus on targeted anti-cancer therapy, *Cancers (Basel)* 12 (2020) 1916, <https://doi.org/10.3390/cancers12071916>.
- [6] U.M. Sonmez, Y.-W. Cheng, S.C. Watkins, B.L. Roman, L.A. Davidson, Endothelial cell polarization and orientation to flow in a novel microfluidic multimodal shear stress generator, *Lab Chip* 20 (2020) 4373–4390, <https://doi.org/10.1039/D0LC00738B>.
- [7] H. Moghadas, M.S. Saidi, N. Kashaninejad, N.-T. Nguyen, Challenge in particle delivery to cells in a microfluidic device, *Drug Deliv. Transl. Res.* 8 (2018) 830–842, <https://doi.org/10.1007/s13346-017-0467-3>.
- [8] K.-J. Jang, K.-Y. Suh, A multi-layer microfluidic device for efficient culture and analysis of renal tubular cells, *Lab Chip* 10 (2010) 36–42, <https://doi.org/10.1039/B907515A>.
- [9] X. Cheng, P.M. Pinsky, The balance of fluid and osmotic pressures across active biological membranes with application to the corneal endothelium, *PLoS One* 10 (2015), e0145422, <https://doi.org/10.1371/journal.pone.0145422>.
- [10] S. Kim, S.C. LeshnerPerez, C. Yamanishi, J.M. Labuz, B. Leung, S. Takayama, Pharmacokinetic profile that reduces nephrotoxicity of gentamicin in a perfused kidney-on-a-chip, *Biofabrication* 8 (2016), 015021, <https://doi.org/10.1088/1758-5090/8/1/015021>.
- [11] N. Kashaninejad, M.R. Nikmaneshi, H. Moghadas, A. Kiyomarsi Oskouei, M. Rismanian, M. Barisam, M.S. Saidi, B. Firoozabadi, Organ-Tumor-on-a-Chip for chemosensitivity assay: a critical review, *Micromachines* 7 (2016), <https://doi.org/10.3390/mi7080130>.
- [12] E.W. Esch, A. Bahinski, D. Huh, Organs-on-chips at the frontiers of drug discovery, *Nat. Rev. Drug Discov.* 14 (2015) 248–260, <https://doi.org/10.1038/nrd4539>.
- [13] M. Yaghoobi, M.S. Saidi, S. Ghadami, N. Kashaninejad, An interface—particle interaction approach for evaluation of the Co-encapsulation efficiency of cells in a flow-focusing droplet generator, *Sensors* 20 (2020) 3774, <https://doi.org/10.3390/s20133774>.
- [14] N. Kashaninejad, M.J.A. Shiddiky, N.-T. Nguyen, Advances in microfluidics-based assisted reproductive technology: from sperm sorter to reproductive system-on-a-chip, *Adv. Biosyst.* 2 (2018) 1700197, <https://doi.org/10.1002/adbi.201700197>.
- [15] N. Ye, J. Qin, W. Shi, X. Liu, B. Lin, Cell-based high content screening using an integrated microfluidic device, *Lab Chip* 7 (2007) 1696–1704, <https://doi.org/10.1039/B711513J>.
- [16] K. Tian, W. Zhong, Y. Zhang, B. Yin, W. Zhang, H. Liu, Microfluidics-based optimization of neuroleukin-mediated regulation of articular chondrocyte proliferation, *Mol. Med. Rep.* 13 (2016) 67–74, <https://doi.org/10.3892/mmr.2015.4540>.
- [17] S.-P. Huang, Y.-J. Chuang, W.-B. Lee, Y.-C. Tsai, C.-N. Lin, K.-F. Hsu, G.-B. Lee, An integrated microfluidic system for rapid, automatic and high-throughput staining of clinical tissue samples for diagnosis of ovarian cancer, *Lab Chip* 20 (2020) 1103–1109, <https://doi.org/10.1039/C9LC00979E>.

- [18] M. Rismanian, M.S. Saidi, N. Kashaninejad, A microfluidic concentration gradient generator for simultaneous delivery of two reagents on a millimeter-sized sample, *J. Flow Chem.* 10 (2020) 615–625, <https://doi.org/10.1007/s41981-020-00104-7>.
- [19] M. Ebadi, K. Moshksayan, N. Kashaninejad, M.S. Saidi, N.-T. Nguyen, A tool for designing tree-like concentration gradient generators for lab-on-a-chip applications, *Chem. Eng. Sci.* 212 (2020) 115339, <https://doi.org/10.1016/j.ces.2019.115339>.
- [20] S.J. Mo, J.-H. Lee, H.G. Kye, J.M. Lee, E.-J. Kim, D. Geum, W. Sun, B.G. Chung, A microfluidic gradient device for drug screening with human iPSC-derived motoneurons, *Analyst* 145 (2020) 3081–3089, <https://doi.org/10.1039/C9AN02384D>.
- [21] M. Rismanian, M.S. Saidi, N. Kashaninejad, A new non-dimensional parameter to obtain the minimum mixing length in tree-like concentration gradient generators, *Chem. Eng. Sci.* 195 (2019) 120–126, <https://doi.org/10.1016/j.ces.2018.11.041>.
- [22] S. Razavi Bazaz, N. Kashaninejad, S. Azadi, K. Patel, M. Asadnia, D. Jin, M. Ebrahimi Warkiani, Rapid softlithography using 3D-printed molds, *Adv. Mater. Technol.* 4 (2019) 1900425, <https://doi.org/10.1002/admt.201900425>.
- [23] F. Eduati, R. Utharala, D. Madhavan, U.P. Neumann, T. Longerich, T. Cramer, J. Saez-Rodriguez, C.A. Merten, A microfluidics platform for combinatorial drug screening on cancer biopsies, *Nat. Commun.* 9 (2018) 2434, <https://doi.org/10.1038/s41467-018-04919-w>.
- [24] M. Astolfi, B. Péant, M. Lateef, N. Rousset, J. Kendall-Dupont, E. Carmona, F. Monet, F. Saad, D. Provencher, A.-M. Mes-Masson, Micro-dissected tumor tissues on chip: an ex vivo method for drug testing and personalized therapy, *Lab Chip* 16 (2016) 312–325, <https://doi.org/10.1039/C5LC01108F>.
- [25] L. Liang, Y. Jin, X. Zhu, F. Zhou, Y. Yang, Real-time detection and monitoring of the drug resistance of single myeloid leukemia cells by diffused total internal reflection, *Lab Chip* 18 (2018) 1422–1429, <https://doi.org/10.1039/C8LC00088C>.
- [26] J. Sun, W. Liu, Y. Li, A. Gholamipour-Shirazi, A. Abdulla, X. Ding, An on-chip cell culturing and combinatorial drug screening system, *Microfluid. Nanofluid.* 21 (2017) 125, <https://doi.org/10.1007/s10404-017-1959-7>.
- [27] C.-W. Chang, Y.-J. Cheng, M. Tu, Y.-H. Chen, C.-C. Peng, W.-H. Liao, Y.-C. Tung, A polydimethylsiloxane–polycarbonate hybrid microfluidic device capable of generating perpendicular chemical and oxygen gradients for cell culture studies, *Lab Chip* 14 (2014) 3762–3772, <https://doi.org/10.1039/C4LC00732H>.
- [28] C. Hu, Y.-S. Lin, H. Chen, J. Liu, F. Nie, Concentration gradient generator for H460 lung cancer cell sensitivity to resist the cytotoxic action of curcumin in microenvironmental pH conditions, *RSC Adv.* 6 (2016) 107310–107316, <https://doi.org/10.1039/C6RA20804E>.
- [29] A.G. Toh, Z. Wang, C. Yang, N.-T. Nguyen, Engineering microfluidic concentration gradient generators for biological applications, *Microfluid. Nanofluid.* 16 (2014) 1–18, <https://doi.org/10.1007/s10404-013-1236-3>.
- [30] B. Hong, P. Xue, Y. Wu, J. Bao, Y.J. Chuah, Y. Kang, A concentration gradient generator on a paper-based microfluidic chip coupled with cell culture microarray for high-throughput drug screening, *Biomed. Microdevices* 18 (2016) 21, <https://doi.org/10.1007/s10544-016-0054-2>.
- [31] D. Park, H. Jeon, M. Kim, X. Nguyen, K. Morten, J. Go, Development of a microfluidic perfusion 3D cell culture system, *J. Micromech. Microeng.* 28 (2018), 045001, <https://doi.org/10.1088/1361-6439/aaa877>.
- [32] H. Wang, T. Li, Y. Bao, S. Wang, X. Meng, A multifunctional integrated simultaneously online screening microfluidic biochip for the examination of “efficacy-toxicity” and compatibility of medicine, *Chin. Chem. Lett.* 30 (2019) 403–405, <https://doi.org/10.1016/j.cclet.2018.08.016>.
- [33] N.-T. Nguyen, S.A.M. Shaegh, N. Kashaninejad, D.-T. Phan, Design, fabrication and characterization of drug delivery systems based on lab-on-a-chip technology, *Adv. Drug Del. Rev.* 65 (2013) 1403–1419, <https://doi.org/10.1016/j.addr.2013.05.008>.
- [34] W. Lim, S. Park, A microfluidic spheroid culture device with a concentration gradient generator for high-throughput screening of drug efficacy, *Molecules* 23 (2018) 3355, <https://doi.org/10.3390/molecules23123355>.
- [35] J.H. Kang, Y.C. Kim, J.-K. Park, Analysis of pressure-driven air bubble elimination in a microfluidic device, *Lab Chip* 8 (2008) 176–178, <https://doi.org/10.1039/B712672G>.
- [36] J. Shemesh, I. Jalilian, A. Shi, G.H. Yeoh, M.L.K. Tate, M.E. Warkiani, Flow-induced stress on adherent cells in microfluidic devices, *Lab Chip* 15 (2015) 4114–4127, <https://doi.org/10.1039/C5LC00633C>.
- [37] K.-J. Jang, A.P. Mehr, G.A. Hamilton, L.A. McPartlin, S. Chung, K.-Y. Suh, D.E. Ingber, Human kidney proximal tubule-on-a-chip for drug transport and nephrotoxicity assessment, *Integr. Biol.* 5 (2013) 1119–1129, <https://doi.org/10.1039/c3ib40049b>.
- [38] M.N. Hsu, G.D.S. Tan, M. Tania, E. Birgersson, H.L. Leo, Computational fluid model incorporating liver metabolic activities in perfusion bioreactor, *Bio-technol. Bioeng.* 111 (2014) 885–895, <https://doi.org/10.1002/bit.25157>.
- [39] K.-Y. Lo, Y. Zhu, H.-F. Tsai, Y.-S. Sun, Effects of shear stresses and antioxidant concentrations on the production of reactive oxygen species in lung cancer cells, *Biomicrofluidics* 7 (2013), 064108, <https://doi.org/10.1063/1.4836675>.
- [40] Z. Tong, L.S.-L. Cheung, K.J. Stebe, K. Konstantopoulos, Selectin-mediated adhesion in shear flow using micropatterned substrates: multiple-bond interactions govern the critical length for cell binding, *Integr. Biol.* 4 (2012) 847–856, <https://doi.org/10.1039/c2ib20036h>.
- [41] E. Westein, A.D. van der Meer, M.J. Kuijpers, J.-P. Frimat, A. van den Berg, J.W. Heemskerk, Atherosclerotic geometries exacerbate pathological thrombus formation poststenosis in a von Willebrand factor-dependent manner, *Proc. Natl. Acad. Sci. U.S.A.* 110 (2013) 1357–1362, <https://doi.org/10.1073/pnas.1209905110>.
- [42] T. Thorsen, S.J. Maerkl, S.R. Quake, Microfluidic large-scale integration, *Science* 298 (2002) 580–584, <https://doi.org/10.1126/science.1076996>.
- [43] M. Barisam, M. Saidi, N. Kashaninejad, N.-T. Nguyen, Prediction of necrotic core and hypoxic zone of multicellular spheroids in a microbio-reactor with a u-shaped barrier, *Micromachines* 9 (2018) 94, <https://doi.org/10.3390/mi9030094>.
- [44] S. Sohrabi, M.S. Saidi, M. Saadatmand, M.H. Banazadeh, B. Firoozabadi, Three-dimensional simulation of urine concentrating mechanism in a functional unit of rat outer medulla. I. Model structure and base case results, *Math. Biosci.* 258 (2014) 44–56, <https://doi.org/10.1016/j.mbs.2014.08.010>.
- [45] M. Kargol, A. Kargol, Mechanistic equations for membrane substance transport and their identity with Kedem–Katchalsky equations, *Biophys. Chem.* 103 (2003) 117–127, [https://doi.org/10.1016/S0301-4622\(02\)00250-8](https://doi.org/10.1016/S0301-4622(02)00250-8).
- [46] B.K. Leung, J.A. Bonanno, C.J. Radke, Oxygen-deficient metabolism and corneal edema, *Prog. Retin. Eye Res.* 30 (2011) 471–492, <https://doi.org/10.1016/j.preteyeres.2011.07.001>.
- [47] P.-O. Gendron, F. Avaltroni, K. Wilkinson, Diffusion coefficients of several rhodamine derivatives as determined by pulsed field gradient–nuclear magnetic resonance and fluorescence correlation spectroscopy, *J. Fluoresc.* 18 (2008) 1093, <https://doi.org/10.1007/s10895-008-0357-7>.